

PAPER

[View Article Online](#)
[View Journal](#) | [View Issue](#)Cite this: *Energy Environ. Sci.*,
2023, 16, 513Probing the stability of SrIrO_3 during active water electrolysis *via operando* atomic force microscopy†Andrew R. Akbashev, ^{a,b,c} Vladimir Roddatis, ^{df} Christoph Baeumer, ^{abe}
Tianchi Liu, ^a J. Tyler Mefford ^{ab} and William C. Chueh ^{ab}

Mechanistic studies of oxide electrocatalysts for heterogeneous water oxidation have been primarily focused on understanding the origins of activity, with fewer studies addressing fundamental properties that influence stability. The main challenge is directly observing and quantifying local structural instability under operating conditions. In this work, we provide a dynamic view of the perovskite stability as a function of time and operational voltage using *operando* electrochemical atomic force microscopy (EC-AFM). Specifically, we study the degradation pathways of SrIrO_3 , a highly active electrocatalyst, during the oxygen evolution reaction (OER) by tracking the potential-dependent Sr leaching and perovskite dissolution at the nanometer scale. This material serves as a model system for degradation studies of perovskite AMO_3 oxides, exhibiting both A-cation leaching and transition metal (M) dissolution. We show that Sr leaching precedes perovskite dissolution by up to 0.8 V, leading to a wide voltage window of stability where water oxidation occurs on a Sr-depleted surface without significant corrosion. Moreover, we reveal that the stability of the perovskite surface is strongly influenced by the electrolytic environment and that corrosion rates differ dramatically as a function of dissolved Sr concentration. Ultimately, our study demonstrates that the overall stability of perovskite oxides during electrocatalysis can be substantially improved by suppressing A-site leaching.

Received 16th November 2022,
Accepted 14th December 2022

DOI: 10.1039/d2ee03704a

rsc.li/ees

Broader context

Oxygen evolution (OER) is an essential reaction in water electrolysis. However, it requires high anodic potentials and promotes oxidation of electrode surfaces beyond their thermodynamic stability limits, leading to surface degradation. Probing the anodic stability during OER is challenging and requires sophisticated approaches. In this work, we employ *operando* electrochemical atomic force microscopy and dynamically probe the stability of perovskite SrIrO_3 (a highly active OER electrocatalyst) on the nanoscale. Our experiments reveal that the degradation of SrIrO_3 involves two steps – Sr leaching and perovskite dissolution that are separated by a wide voltage gap. This observation implies that an intense OER can occur on Sr-depleted surface without its significant corrosion. We also found that the stability of the perovskite surface is strongly influenced by the presence of Sr^{2+} in the electrolyte. Ultimately, the study shows that suppression of A-site leaching from a perovskite ABO_3 is vital for its improved anodic stability.

Introduction

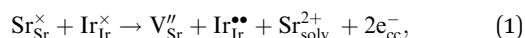
During water electrolysis, hydrogen is produced through electrochemical reduction of water at the cathode while the anode oxidizes water to oxygen *via* the oxygen evolution reaction (OER). Due to their high OER activity, perovskite oxides containing transition metals are among the most attractive electrocatalytic materials for water oxidation.^{1,2} However, during OER, perovskites experience corrosive degradation through the formation of oxidized and water-soluble transition metal species on the surface.^{3–10} A lack of fundamental understanding of how structure and composition of perovskite surfaces evolves during OER and which mechanisms drive their electrochemical

^a Department of Materials Science and Engineering, Stanford University, Stanford, CA 94305, USA. E-mail: andrei.akbashev@psi.ch^b Stanford Institute for Materials and Energy Sciences, SLAC National Accelerator Laboratory, Menlo Park, CA 94025, USA^c Division for Research with Neutrons and Muons, Paul Scherrer Institute, 5232 Villigen, Switzerland^d German Research Centre for Geosciences GFZ, Helmholtz Centre Potsdam, 14473 Potsdam, Germany^e Institute of Electronic Materials (IWE2) and JARA-FIT, RWTH Aachen University, 52062 Aachen, Germany^f Institute of Materials Physics, University of Göttingen, 37077 Göttingen, Germany† Electronic supplementary information (ESI) available. See DOI: <https://doi.org/10.1039/d2ee03704a>

degradation poses a significant challenge to the development of stable and active electrocatalysts.^{11–14}

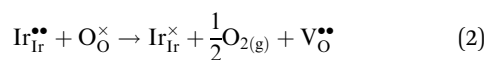
Several major pathways for the electrochemical degradation of perovskite electrocatalysts have been proposed. First, selective leaching of alkali-earth metals during the OER on perovskite surfaces is ubiquitous. Under oxidative conditions, such A-site cation-depleted surface layers eventually drive structural transformation and amorphization.^{3,4} Second, oxidative dissolution of transition metals from oxide surfaces is often observed at high overpotentials.^{7,13,15,16} The rate of such anodic dissolution strongly depends on the chemical composition,^{7,12,17–19} structure^{19,20} and crystallographic orientation¹⁶ (facet) of the oxide surface. Finally, the evolution of lattice oxygen modifies the ligand coordination of surface transition metal ions, becoming an additional factor in the degradation of a perovskite.^{21–23} For clarity, we define leaching as an ion de-insertion process that preserves the structural motif of an oxide (*i.e.*, a topochemical reaction involving vacancies), while dissolution is a complete structural disintegration of the surface layer through the solvation of the transition metal ions.

Strontium iridate (SrIrO₃) has recently attracted attention owing to its exceptionally high OER activity proposed to originate through Sr²⁺ leaching and surface amorphization.^{3,7,8,10,24–28} Assuming that Sr²⁺ leaching involves electrochemical de-insertion (Path 1 as opposed to Path 2 in eqn (S1), ESI[†]), electrochemical leaching of Sr²⁺ from SrIrO₃ involves two holes (h[•]). The reaction in the Kröger-Vink notation is as follows (see also eqn (S1), ESI[†]):

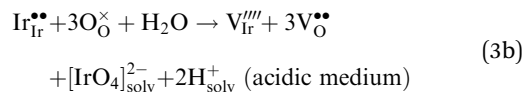
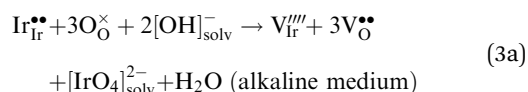


where “cc” means current collector and “solv” means the species is in the solvated state (in solution). This reaction creates a surface layer of Sr_{1–x}IrO₃ proposed to contain Ir(vi). Previous studies showed that Sr leaching leads to the formation of an OER-active defect-rich IrO_x surface layer in acidic electrolytes.^{8,10}

Depending on pH and applied potential, additional reactions may occur after Sr leaches out. One possibility is that the Sr-deficient layer evolves lattice oxygen chemically (no net electron transferred) *via* the reaction that restores Ir(iv) within the near-surface layer:



When put together, eqn (1) and (2) comprise the formation of a partial Schottky defect $\text{V}_{\text{Sr}}^{\prime\prime} + \text{V}_{\text{O}}^{\bullet\bullet}$. Another possibility is that Ir_{Ir}^{••} dissolves chemically through the solvation of the [IrO₄]^{2–} species:



One can note that adding eqn (1) and (3) yields the electrochemical dissolution reaction under the assumption that the vacancies are generated at the surface and become eliminated as a lattice unit. Although several scenarios were proposed previously,^{14,17,18,29} the mechanism involving the dissolution of Ir(vi) oxide is the most probable at high potentials because IrO₃ is volatile and soluble in water.^{30–32} Anodic dissolution of iridium during OER was observed for both metallic iridium^{12,17,33–35} and Ir-containing oxides such as hydrous/amorphous^{11,19,35} and rutile IrO₂,^{11,12,19,33} perovskite SrIrO₃,¹⁹ double-perovskite Sr₂CoIrO₆⁷ and Ba₂PrIrO₆.¹⁹ We also note that this scenario can lead to the growth of amorphous and possibly hydrated IrO_x on the surface through a precipitation reaction.⁷

While Sr leaching and iridium dissolution have been investigated separately, the coupling between the two processes is poorly understood because both Sr leaching and surface evolution are inherently dynamic processes and cannot be characterized using *post mortem* measurements that provided a static (*ex situ*) insight. Employing SrIrO₃ as a model system, in this work we study the oxidative electrochemical behavior of a perovskite electrocatalyst in real time, demonstrating that corrosion of a perovskite is not a simple “layer-by-layer” process hypothesized earlier³⁶ but involves many processes that precede dissolution and influence activity and stability. Specifically, we reveal that the perovskite dissolution initiates at potentials that are significantly higher than those for Sr leaching. We also show that the dissolution can be controlled by suppressing the Sr leaching rate using the Sr²⁺-containing electrolyte.

Experimental results

Single-crystalline surfaces were prepared by depositing SrIrO₃ epitaxial thin films on Nb-doped (001) SrTiO₃ substrates using pulsed laser deposition. The samples were grown in a layer-by-layer mode and exhibit high crystalline quality and step terraces at the surface. To quantify film thickness in AFM experiments, we fabricated a Sr₃Al₂O₆ lift-off pattern prior to SrIrO₃ deposition, creating a sharp step between the film and the substrate (Fig. S3, ESI[†]). As our samples showed a potential-dependent solid-state junction resistance, no *iR* correction was performed on the electrochemical data, which affects mostly the potential regions involving high currents and measured in the rotating disk electrode (RDE) cell (specific values for the solution resistance are in Methods). Here, we also comment on the variability of long-term stability of the SrIrO₃ electrodes reported in literature. In previous studies, different behaviors of SrIrO₃ films in acidic electrolytes were reported, including (i) a small increase of activity during the first sweeps followed by degradation,⁸ (ii) a moderate and continuous increase in activity without any noticeable dissolution of the film,²⁷ (iii) a

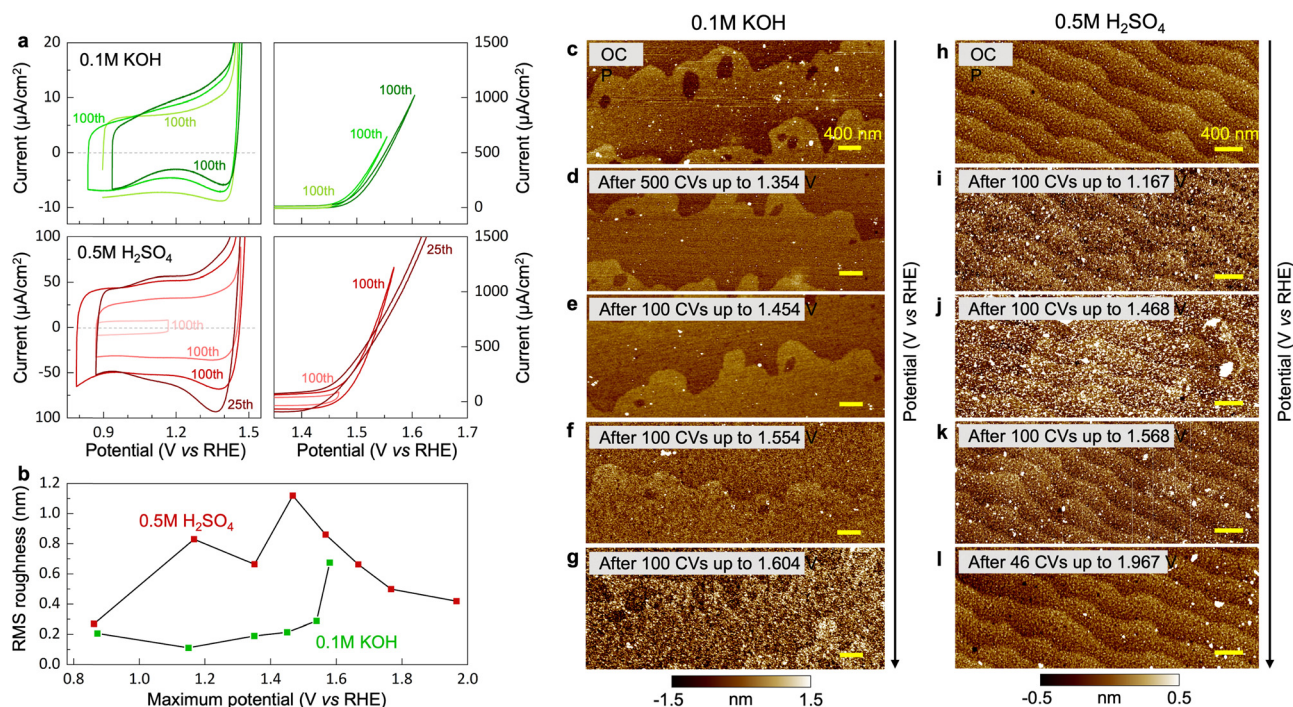


Fig. 1 (a) Capacitive (left) and OER (right) regions of the SrIrO₃ film after a given number of cycles up to different anodic given potentials measured in the RDE cell. No *iR* correction was made because our samples showed a potential-dependent solid-state junction resistance (see Methods). (b) The root mean square (RMS) roughness after each CV series up to a maximum potential in 0.1 M KOH and 0.5 M H₂SO₄. (c)–(l) Surface roughening during cycling up to increasingly higher potentials in 0.1 M KOH and 0.5 M H₂SO₄, corresponding to CV conditions given in (a) and (b) (scale bars are 400 nm). The open-circuit potential, OCP, was near 0.9 V vs. RHE. See Fig. S6 and S8 (ESI†) for further data and information.

significant increase of activity during a galvanostatic test.¹⁰ In our study, we do not see activity improvement in either prolonged cycling or galvanostatic tests (Fig. S5 and S16, ESI†). This difference is likely due to our films being substantially more atomically flat than those presented in literature.

First, we performed cyclic voltammetry in 0.1 M KOH (pH = 12.8) and 0.5 M H₂SO₄ (pH = 0.29) electrolytes followed by *ex situ* AFM to characterize the surface morphology (Fig. 1). In KOH, the dissolution of SrIrO₃ starts at the observable onset of OER (1.45 V vs. RHE, reversible hydrogen electrode), as evidenced by the decrease in film thickness (Fig. S7, ESI†). Importantly, AFM images show that the step terraces remain topographically preserved, and electrochemical dissolution does not follow a step retreat^{37,38} or etch pit formation^{39,40} which are prevalent during chemical dissolution of crystals. Instead, the film dissolves uniformly, with step terraces remaining topographically visible even after the total height loss of 5 nm (Fig. 1(c)–(g) and Fig. S6, S7, ESI†), with roughness simultaneously increasing with the amount of dissolved film (Fig. 1(b)). While it is not possible to map OER activity at a nanometer resolution, we hypothesize that the plateaus dominate the observed OER response as the performance does not correlate with surface roughness (as shown in Fig. 1). Still, we hesitate to draw a conclusion here without direct observation. In H₂SO₄, on the other hand, no dissolution is observed under these potentials (as shown by *operando* EC-AFM and discussed below). Instead, particulates appear at ~1.17 V and disappear

at 1.5–1.6 V (Fig. 1(h)–(l)). Most of such particulates are < 5 nm in size, but some reach over 20 nm. These particulates noticeably impact the surface roughness (Fig. 1(b)) but do not change the overall step-terraced morphology. We note that some particulates were observed in KOH as well, but they were more sparsely distributed than in H₂SO₄.

Next, we employed *operando* EC-AFM to track the dissolution kinetics of SrIrO₃ by quantifying the potential-dependent topography and thickness. Specifically, the tip scans fast perpendicular to the edge between the exposed substrate region and SrIrO₃ electrode and generates a height profile of the film relative to the substrate. The slow scan direction is parallel to the edge and is correlated in time to the concurrent linear sweep voltammetry (LSV) measurement (Fig. S3b, ESI†). In KOH, as the potential reaches 1.3–1.4 V, the SrIrO₃ surface develops particulates that extend tens of nm laterally and only few nm in height (Fig. 2(a), (b) and Fig. S9, ESI†). These particulates are immobile when scanned with an AFM tip and disappear as SrIrO₃ starts to dissolve at ~2 V (Fig. 2(a) and Fig. S9, S11, S12, ESI†). We speculate that these particulates are SrCO₃, a reaction product between leached Sr²⁺ and dissolved CO₃²⁻. The CO₃²⁻ species are dominant at high pH⁴¹ and originate from the dissolved CO₂ in the electrolyte that is exposed to air. At pH = 12.8, the Sr²⁺ solubility (in equilibrium with SrCO₃) is only 23 μM. Another possibility is chemical precipitation^{42,43} of IrO_x·nH₂O at high pH from the hydrolyzed species of Ir(III) or Ir(IV) (such as [Ir(OH)₅(H₂O)]²⁻ or

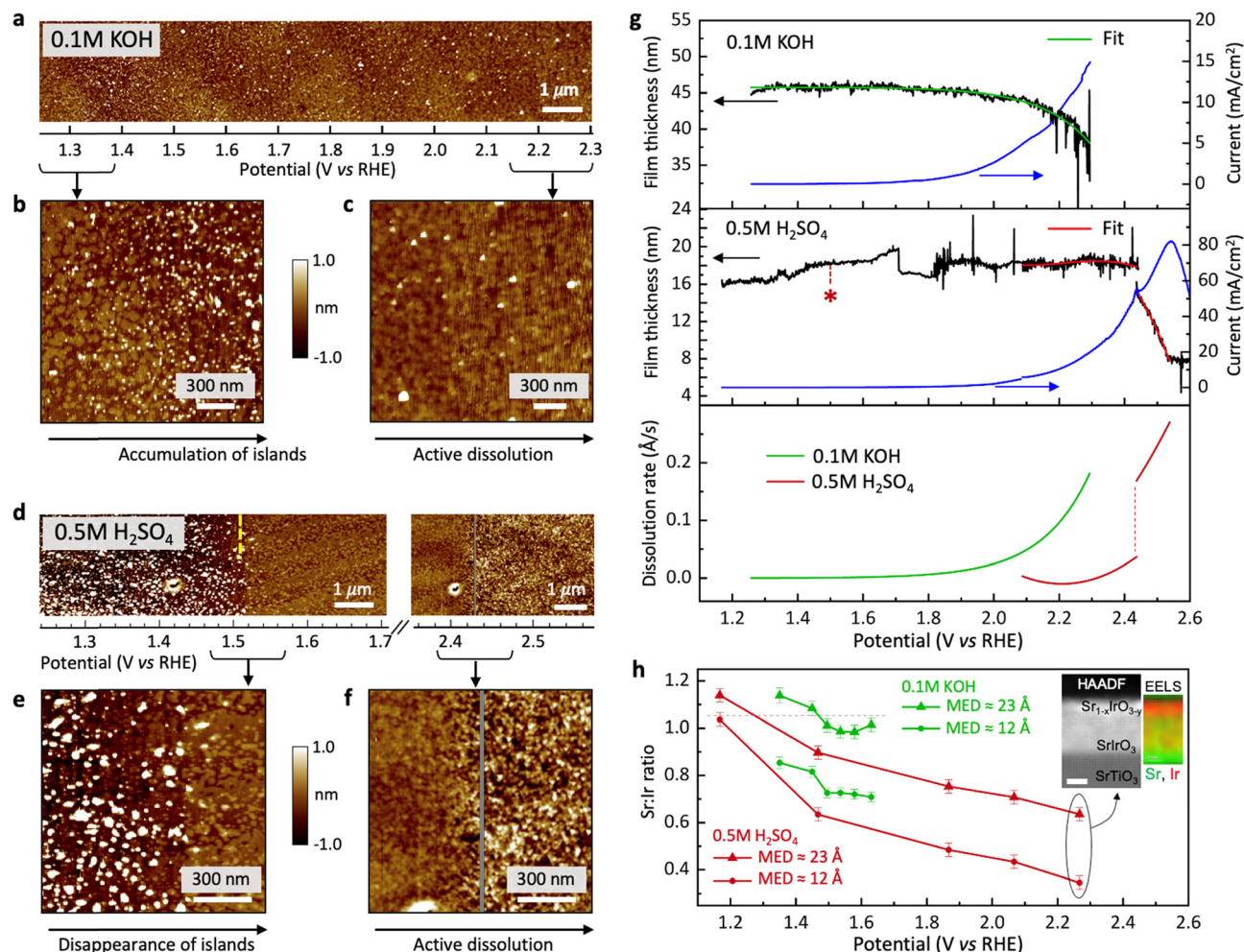


Fig. 2 (a) *Operando* EC-AFM measurements of the SrIrO_3 film in 0.1 M KOH (see also Fig. S9, ESI†). (b) and (c) An enlarged region of the AFM image showing (b) the initiation of the potential-dependent surface evolution that generates particulates on the surface without the loss of the step-terraced surface morphology, and (c) the dissolution regime (the image is flattened for clarity). (d) The evolution of the SrIrO_3 film in 0.5 M H_2SO_4 . The plot does not show several spikes associated with poor contact and tip disengagement (see Fig. S10, ESI† for more information). (e) and (f) Disappearance of particulates from the surface and the beginning of active dissolution of $\text{Sr}_{1-x}\text{IrO}_3$. (g) Evolution of the film thickness with potential in 0.1 M KOH and 0.5 M H_2SO_4 obtained in the *operando* EC-AFM experiment. The dissolution rate is evaluated by fitting the thickness as a function of time (green curve – exponential fit, red curve – 3rd degree polynomial fit). The red asterisk marks the potential at which the particulates on the surface in (d) disappear (yellow dashed line). (h) X-ray photoelectron spectroscopy showing Sr depletion at the surface near the OER onset potential for the two electrolytes. MED – mean escape depth. The error bars represent standard deviation in percentage (derived from the standard deviation of five XPS measurements performed on an as-grown film). The Sr : Ir ratio from XPS is higher than it is in the film due to the presence of Sr-containing particulates on the surface. The inset shows the HAADF STEM image and EELS map of the film after the *ex situ* XPS measurements in 0.5 M H_2SO_4 revealing a heavily Sr-depleted surface $\text{Sr}_{1-x}\text{IrO}_{3-y}$ layer. The scale bar is 3 nm.

$[\text{Ir}(\text{OH})_6]^{2-}$). However, we do not see such particulates at higher potentials when the concentration of anodically dissolved iridium reaches the highest value in the solution.

In H_2SO_4 , the behavior of SrIrO_3 is markedly different. Fig. 2(d) shows the evolution of the topography, thickness, and current density during a slow LSV sweep measured with EC-AFM. The particulates appear at potentials close to open-circuit and remain on the surface until ~ 1.5 V (Fig. 2(e)), consistent with *ex situ* AFM imaging (Fig. 1(h)–(l)). We propose that these particulates are SrSO_4 , with the solubility limit of Sr^{2+} being $24 \mu\text{M}$.

Finally, we turn our attention to the evolution of the electrode thickness. The potential-dependent dissolution rates in

both alkaline and acidic electrolytes extracted from the AFM data are plotted in Fig. 2(g). The onset potential of dissolution in KOH is 1.9–2.0 V, with the rates reaching 0.2 Å s^{-1} at 2.3 V. In H_2SO_4 the onset potential is substantially higher at 2.4 V.

To understand the evolution of chemical composition in the near-surface layer, we performed X-ray photoelectron spectroscopy (XPS) after a 5 min potentiostatic hold at different potentials spanning both the pre-catalytic and OER regions. We note that XPS can show higher Sr : Ir ratio than it is in the film due to the abundant particulates on the surface that contribute to the overall Sr signal. In XPS, the Sr : Ir molar ratio was probed for two distinct mean escape depths (MED): (i) surface region having MED $\approx 12 \text{ Å}$ for Sr and 12 Å for Ir,

and (ii) thicker (deeper) surface layer with MED ≈ 23 Å for Sr and 24 Å for Ir. Specifically, we found that Sr leaching in KOH proceeds from 1.3 to 1.5 V, after which the Sr:Ir ratio levels off and remains constant (Fig. 2(h)). The loss of Sr coincides with the appearance of particulates on the surface, consistent with our hypothesis of a “leaching-precipitation mechanism” whereby a critical concentration of leached Sr^{2+} reacts with CO_3^{2-} to form SrCO_3 . Most crucially, Sr leaching occurs at a potential ~ 0.3 V lower than the onset of dissolution.

In H_2SO_4 , Sr leaching is also observed but it does not level off with potential (Fig. 2(h)). Instead, the Sr:Ir ratio at MED ≈ 12 Å decreases to 0.35 close to the onset of dissolution at 2.3 V, forming a substantially more Sr-depleted surface than in KOH. The inset in Fig. 2(h) shows high-angle annular dark field (HAADF) scanning transmission electron microscopy (STEM) images and the distribution of Sr and Ir obtained by mapping the electron energy loss spectra (EELS) in the film after the last measurement. The images reveal a highly disordered strontium-deficient $\text{Sr}_{1-x}\text{IrO}_{3-y}$ layer (~ 3 –4 nm thick) on top of SrIrO_3 . These results directly correlate with the XPS data. Similar layers were observed previously for SrIrO_3 in HClO_4 ²⁷ and H_2SO_4 .^{8,10,24} Importantly, by comparing Fig. 2(g) and Fig. 2(h), we observe a large potential gap (~ 0.6 V) between Sr leaching and perovskite dissolution.

To probe the bulk dissolution process, we perform *operando* EC-AFM galvanostatically at 10 mA cm^{-2} in both alkaline and acidic electrolytes. The potential required to drive such high currents in the AFM liquid cell is greater than the potential measured in the RDE experiments due to uncompensated

resistance losses in the constrained geometry inside the AFM cell. In KOH, the film dissolution rate measured directly *via operando* EC-AFM is $\sim 0.1\text{ Å s}^{-1}$ and remains constant with thickness (Fig. 3(a)). Particulates like those observed in slow LSV appear immediately after the potential is reached (Fig. S13 and S14, ESI†). In H_2SO_4 , on the other hand, EC-AFM shows no detectable dissolution of the film over a period of 80 min (Fig. 3(b) and Fig. S15, ESI†), indicating a much higher stability at 10 mA cm^{-2} than in the case of alkaline electrolyte.

In the final set of experiments, we test our hypothesis that Sr leaching promotes a faster dissolution of the perovskite phase. Specifically, we measure nominally identical SrIrO_3 electrodes (30 nm thick) galvanostatically at 10 mA cm^{-2} in various electrolytes using a rotating disk electrode in a large volume cell (Fig. 3(c)). A rapid increase of potential beyond 3 V indicates a complete dissolution of the film. First, we perform these experiments in KOH and H_2SO_4 . In KOH, SrIrO_3 shows a short 60-min plateau at ~ 1.8 V, indicating that the dissolution rate is 0.08 Å s^{-1} and consistent with the EC-AFM results. In H_2SO_4 , the film shows two plateaus: one at ~ 1.67 V with a longer stability than in the basic electrolyte and the second plateau at ~ 2.32 V that continues for ~ 500 min. The resulting dissolution rate of 0.006 Å s^{-1} is ~ 10 times smaller than in KOH and correlates well with a negligible dissolution rate reported for IrO_2 in acids.^{12,22,33} Next, we hypothesize that Sr leaching can be suppressed by decreasing the Sr chemical potential difference between the film and electrolyte. To test this hypothesis, we use a 0.05 M Sr(OH)_2 electrolyte which has the same pH as that of 0.1 M KOH . The galvanostatic test in

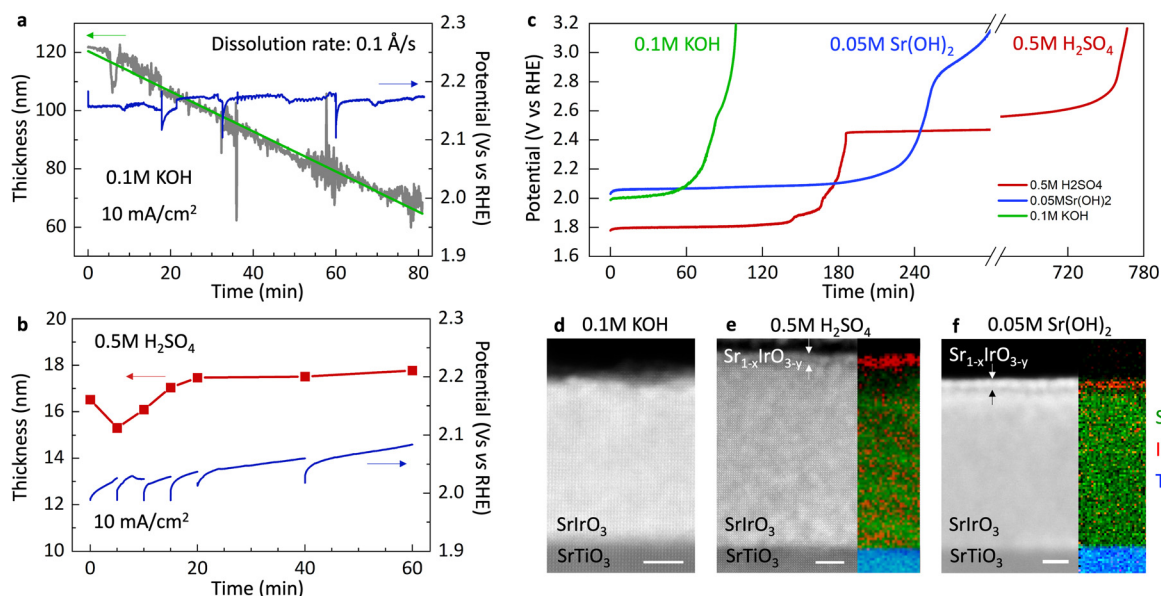


Fig. 3 (a) and (b) Thickness variation of the SrIrO_3 film during galvanostatic measurements at 10 mA cm^{-2} in 0.1 M KOH and $0.5\text{ M H}_2\text{SO}_4$ obtained in *operando* EC-AFM experiments (see more data in Fig. S13–S15, ESI†). (c) Evolution of potential in galvanostatic measurements (at 10 mA cm^{-2}) in an RDE cell showing the variation of OER current as SrIrO_3 films with identical thickness (30 nm) undergo anodic corrosion in different electrolytes. No *iR* correction was made because our samples showed a potential-dependent solid-state junction resistance (see Methods). (d)–(f) HAADF images and EELS maps of the cross sections of the films tested galvanostatically at 10 mA cm^{-2} for 1 h in different electrolytes (scale bar is 5 nm). Initial thicknesses were: (d) 120 nm, (e) 30 nm, (f) 50 nm. Colored EELS maps show Sr (green), Ir (red) and Ti (blue) elemental distribution. Because of the difference in dissolution rates in these electrolytes, the starting thickness of the films was not the same.

$\text{Sr}(\text{OH})_2$ reveals a 2–3 times longer plateau that scales with the film thickness (Fig. 3(c) and Fig. S16, ESI†), while XPS studies indicate a larger Sr:Ir ratio than in the case of KOH and H_2SO_4 (Fig. S17, ESI†). The results of the post-mortem STEM study of the films tested galvanostatically at 10 mA cm^{-2} for 1 h are shown in Fig. 3(d)–(f). In H_2SO_4 and $\text{Sr}(\text{OH})_2$, HAADF-STEM clearly reveals a thin Sr-depleted layer at the surface of the films tested. In KOH, however, no such layer is observed.

Discussion

First, our experiments demonstrate that the onset of Sr leaching and noticeable SrIrO_3 dissolution are separated by a wide potential gap (0.6–0.8 V in H_2SO_4 and 0.3 V in KOH), indicating that $\text{Sr}_{1-x}\text{IrO}_{3-y}$ dissolves only after sufficient Sr leaches from the near-surface region. When compared to literature, this $\text{Sr}_{1-x}\text{IrO}_{3-y}$ layer exhibits higher anodic stability (lower dissolution rate at similar potentials) compared to Ir metal in both alkaline³⁴ and acidic³⁴ conditions, and hydrous Ir oxide in an acid.¹⁸ Since we also see a multifold improvement of the electrode stability in the $\text{Sr}(\text{OH})_2$ electrolyte, we conclude that the anodic stability of perovskites in alkaline electrolytes depends on the amount of Sr within the surface layer (Fig. 4). The more Sr remains in the perovskite structure, the more stable the surface is towards dissolution. In other words, Sr leaching not only precedes perovskite dissolution, but it also controls the anodic stability during OER.

Second, our experiments show that Sr leaching occurs before OER (by $\sim 0.3 \text{ V}$ in H_2SO_4 and 0.1 V in KOH).

These observations do not support the scenario proposed by Wan *et al.*²⁷ whereby Sr leaching in SrIrO_3 happens during OER due to the lattice oxygen oxidation reaction. Instead, we propose that Sr leaching in the pre-OER region can occur *via* the electrochemical deintercalation of Sr^{2+} in both types of electrolytes that is compensated by an increase of the Ir oxidation state (see detailed reactions in eqn (1)).

Third, our *operando* EC-AFM experiments reveal that the SrIrO_3 dissolves in KOH at potentials very close to those in H_2SO_4 . At a dissolution rate of 0.2 \AA s^{-1} (equivalent to $50 \text{ pmol s}^{-1} \text{ cm}^2$), Fig. 2, the potential difference is only 0.2 V, similar to previous observations using on-line electrochemical mass spectrometry for Ir metal.³⁴ In contrast, the Pourbaix diagram shows that the potentials that separate IrO_2 and $[\text{IrO}_4]^{2-}$ stability regions differ by as much as $\sim 0.7 \text{ V}$ between the acidic and basic conditions.^{34,44} This implies that the dissolution of Ir-based oxides is largely governed by the kinetics and cannot be analyzed purely within a thermodynamic framework. The associated reactions in both acidic and alkaline electrolytes are proposed in eqn (2). Alternatively, different stoichiometry of proton-coupled reactions should be considered, moving the dissolution potentials closer to each other.

Finally, we should note that, in contrast to several previous studies, we do not observe an increase in electrocatalytic activity in an acidic electrolyte with time. While the reasons for such a drastically different behavior of SrIrO_3 is unknown, it could be related to a high sensitivity of the surface chemical composition to the deposition conditions of oxide films.⁴⁵

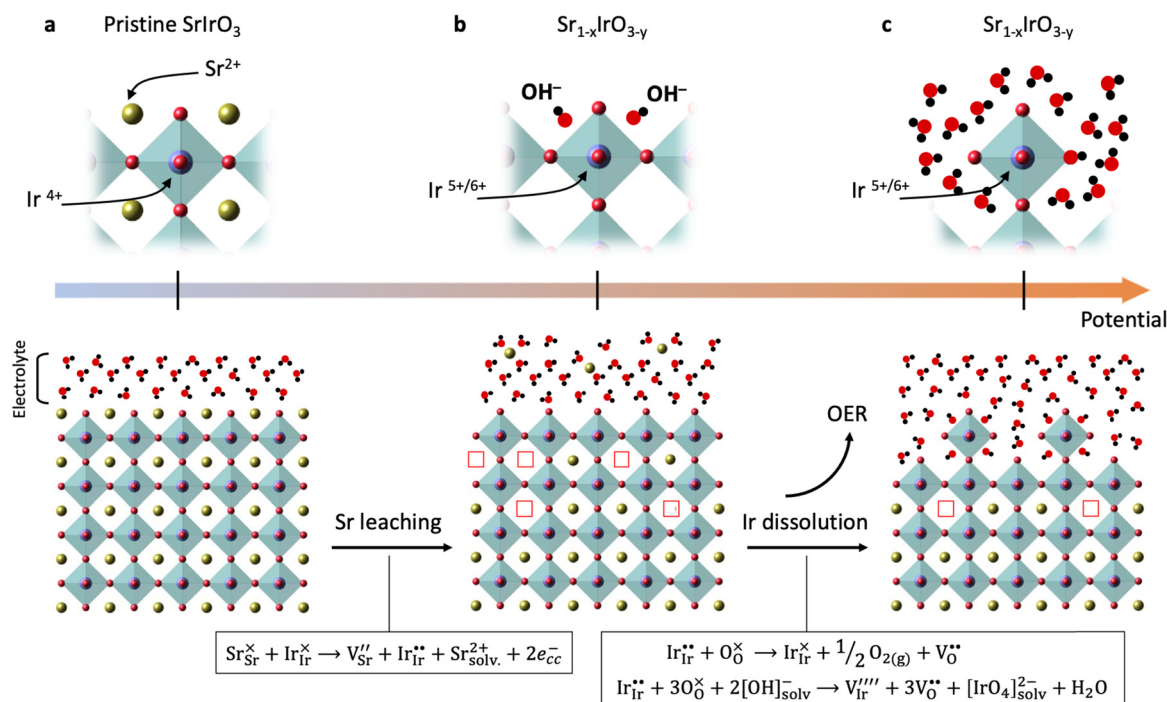


Fig. 4 Strontium leaching as a vital reaction step that leads to the perovskite anodic degradation in an alkaline medium: (a) pristine SrIrO_3 surface in contact with electrolyte; (b) Sr leaching leads to the formation of $\text{Sr}_{1-x}\text{IrO}_3$ with a higher oxidation state of Ir within the near-surface layer; (c) $\text{Ir}^{5+/6+}$ either reduces chemically to Ir^{4+} while evolving O_2 or dissolves *via* hydroxylation and formation of $[\text{IrO}_4]^{2-}$ species.

Conclusion

In this study, we use *operando* EC-AFM to characterize the surface and thickness evolution of model SrIrO₃ electrocatalysts. We quantify the potential-dependent dissolution rate with a sub-nanometer precision across a wide potential range extending deep into the OER region. Our study illustrates the complexity of the pH-dependent interplay between the perovskite dissolution kinetics and Sr leaching during OER. This is further supported by the fact that, in contrast to previous studies, we do not observe an increase of electrocatalytic activity under continuous operation in acidic electrolyte. Importantly, we reveal that Sr leaching precedes the net perovskite dissolution by >0.6 V in H₂SO₄ and 0.3 V in KOH. By inhibiting Sr leaching in the Sr(OH)₂ electrolyte, we demonstrate that the lifetime of the perovskite electrocatalyst is noticeably improved. Our work not only develops new methods for studying the kinetics of electrochemical degradation of oxides, but also shows that the control over the A-site leaching is a viable strategy for achieving improved stability of perovskite electrocatalysts.

Methods

Thin film preparation and characterization

Thin films of SrIrO₃ were grown by pulsed laser deposition (PLD/MBE 2300, PVD Products) on 10 × 10 mm² (001) Nb-doped SrTiO₃ (0.5 wt% doping) (Shinkosha Co., Japan) using SrIrO₃ target (Toshiba Manufacturing, Japan). All substrates were first etched with buffered HF solution (pH = 4.5) and annealed at 950 °C under Argon flow for 2 hours to restore high-quality step terraces. The growth temperature was 700 °C under oxygen pressure of 30 mTorr (some samples were grown under 15 mTorr). The target to substrate distance was 84 mm, the laser fluence was 2 J cm⁻². The growth was monitored *in situ* using a RHEED system (TorrRHEED, Staib Instruments) operated at 35 kV (1.5 mA). The samples with the SrIrO₃-SrTiO₃ step were prepared through the following steps: (i) a small area on the substrate was covered with acetone-soluble photoresist (Megaposit SPR3612); (ii) an amorphous layer (20–30 nm) of water-soluble Sr₃Al₂O₆ was grown at room temperature in the PLD from the Sr₃Al₂O₆ in-house prepared target; (iii) the photoresist was then removed using acetone, leaving a clean area on the substrate; (iv) SrIrO₃ layer was grown on top of the entire sample under conditions mentioned above; (v) finally, the sample was immersed in water for several hours and lightly sonicated to dissolve Sr₃Al₂O₆ and remove the SrIrO₃ layer grown above it but leaving the SrIrO₃ layer in the area previously protected by the photoresist. Such samples had a small area (0.1–0.3 mm²) of the SrIrO₃ film on a large-area substrate and were used in the majority of electrochemical AFM experiments. Although we did not notice any thickness dependence of degradation, thicker films were used in EC-AFM experiments conducted in KOH because of higher dissolution rates of SrIrO₃ in this electrolyte. X-ray diffraction and X-ray reflectivity of thicker films were collected using PANalytical X'Pert PRO

diffractometer equipped with a double monochromator and operating in the parallel-beam geometry.

Transmission electron microscope specimens were prepared by focused ion beam lift-out technique using a Thermofisher Scientific Helios 4G UC instrument operated at 30 kV at the beginning of preparation, followed by 5 and 2 kV for the final cleaning. The HAADF and EELS images were collected with a Thermofisher Scientific (formerly FEI) image-corrected Titan 80–300 environmental TEM operated at 300 kV, equipped with a Gatan Imaging Filter Quantum 965 ER. Another set of specimens was analyzed with a Thermofisher Scientific probe-corrected Themis Z microscope operated at 80 kV and equipped with a Gatan Imaging Filter Continuum 1065 ER.

The air-free XPS characterization was performed with a PHI Versa Probe (Physical Electronics Inc.) with Al K α X-ray illumination, a pass energy of 23.5 eV and at various photoemission angles without neutralization. The samples were first tested electrochemically in the RDE cell inside a nitrogen-filled glove-box and transferred to XPS in a transfer vessel without air exposure. The Sr:Ir stoichiometry was calculated using integrated intensity of the respective peaks after subtraction of the Shirley background in CasaXPS and using the sensitivity factors of 5.7772 (Sr) and 16.1333 (Ir). The mean escape depth was defined through the inelastic mean free path (IMFP) of the photoelectrons λ and the photoemission angle θ through $d = \lambda \times \cos \theta$.⁴⁶ IMFP was calculated to be 23.8 Å for Sr and 24.7 Å for Ir using QUASES-IMFP-TPP2M.⁴⁷ This isotropic approach uses the straight-line approximation,⁴⁸ as is suitable in the absence of well-characterized, material-specific angle-dependent effective attenuation lengths. For a full description of the information depth in photoemission, the readers are referred to the literature.^{46,48,49}

Electrochemical measurements

Electrochemical measurements of the thin films were performed using a rotating disk electrode (RDE, Pine Research) setup at rotation rates of 1000–1500 rpm. A PTFE cell was used and the electrolyte was never exposed to glass. Only the front side of the film was exposed to the electrolyte (film area is 10 × 10 mm², while the electrolyte-contacted area is circular with a diameter of 7.5 mm), and the potential was controlled using a BioLogic SP-300 potentiostat. On the electrolyte side, a film area of 0.75 mm diameter was exposed to the electrolyte and sealed using an O-ring (FFKM, Marco Rubber). Electrical contact was made from the back of the substrate, where the Ti(5 nm) and Pt(50–100 nm) layers were deposited beforehand. The O₂-saturated electrolyte solutions used in the experiments were prepared using the following chemicals: KOH pellets (Sigma-Aldrich, Semiconductor grade, 99.99%), concentrated H₂SO₄ (Honeywell, TraceSELECT™ Ultra), Sr(OH)₂·8H₂O (Alfa Aesar, 99%). A set of carefully maintained Hg/HgO reference electrodes (CHI152, CH Instruments) filled with 1 M KOH were used in the experiments involving alkaline and neutral electrolytes, with a separate “master” electrode that was used for calibration purposes (typical deviations were within 1–3 mV). The 1 M KOH electrolyte inside the Hg/HgO electrode was

replaced after each measurement in the chemically non-native $\text{Sr}(\text{OH})_2$ electrolyte. Similarly, $\text{Hg}/\text{Hg}_2\text{SO}_4$ reference electrodes (RREF0025, Pine Research) were used in the 0.5 M H_2SO_4 . We found that our heterostructures exhibit a solid-state film-substrate junction resistance that is potential-dependent. This makes an accurate correction for resistance difficult. As a result, no correction for the resistance-induced potential drop was done for all samples (the data are as measured). Unless stated otherwise, the solution resistances were (1) in the RDE cell: 54 Ohm in 0.1 M KOH and 8 Ohm in 0.5 M H_2SO_4 , and (2) in the AFM cell: ~ 16 – 20 Ohm in 0.1 M KOH and ~ 4 Ohm in 0.5 M H_2SO_4 . The concentration of Sr^{2+} in equilibrium with SrCO_3 was calculated using the solubility constant $K_{\text{sp}}(\text{SrCO}_3) = 5.6 \times 10^{-10}$ (ref. 50) and with SrSO_4 using the solubility constant $K_{\text{sp}}(\text{SrSO}_4) = 2.33 \times 10^{-7}$ (ref. 51).

Electrochemical atomic force microscopy

Atomic force microscopy was performed using Oxford Instruments Asylum Cypher ES scanning probe microscope and a modified liquid cell. The scans were recorded in a tapping mode using Olympus AC55TS tips (radius ~ 7 nm) that were excited photothermally (blueDriveTM) on the gold-coated reflex side. These tips can operate in liquid at high resonance frequency (~ 1 MHz), have a stable resonance and therefore are ideal for high-resolution imaging. In the scanning process, the phase was kept close to 70–80% to make sure the tip operated in a repulsive regime without a significant mechanical force. The Asylum software package implemented into Igor Pro was used for flattening and correcting the AFM images. When particulates appeared on the surface, depending on the tip-sample interaction, the tip could go afloat. When such lines were occasional, they were removed from the scan using the “Erase line” function under “Modify Panel” in the Asylum software. When the lines were not occasional, they were left as is.

Electrochemical AFM experiments were done in the original liquid cell from Asylum Research but modified to incorporate all three electrodes, one of which was a real reference electrode (Hg/HgO for 0.1 M KOH and $\text{Hg}/\text{Hg}_2\text{SO}_4$ for 0.5 M H_2SO_4). During the OER reaction inside the AFM cell, a continuous electrolyte flow was maintained using a “push-pull” combination of two syringe pumps (PHD ULTRA, Harvard Apparatus) at a rate of 50–500 $\mu\text{L min}^{-1}$ depending on the current.

Conflicts of interest

There are no conflicts to declare.

Acknowledgements

A. R. A., C. B., J. T. M., and W. C. C. acknowledge funding provided by the U.S. Department of Energy (DOE), Office of Basic Energy Sciences, Division of Materials Sciences and Engineering (contract DE-AC0276SF00515). Part of this work was performed at the Stanford Nano Shared Facilities

(SNSF)/Stanford Nano-fabrication Facility (SNF), supported by the National Science Foundation under award ECCS-1542152. V. R. acknowledges the European Regional Development Fund and the State of Brandenburg for the Themis Z TEM (part of the Potsdam Imaging and Spectral Analysis Facility (PISA)), and the use of equipment in the Collaborative Laboratory and User Facility for Electron Microscopy (CLUE) at University of Göttingen. The financial support by the Deutsche Forschungsgemeinschaft, grant number CRC 1073 (Projects Z02) is highly appreciated.

References

- 1 J. Hwang, *et al.*, Perovskites in catalysis and electrocatalysis, *Science*, 2017, **358**, 751–756.
- 2 W. T. Hong, *et al.*, Toward the rational design of non-precious transition metal oxides for oxygen electrocatalysis, *Energy Environ. Sci.*, 2015, **8**, 1404–1427.
- 3 K. J. May, *et al.*, Influence of Oxygen Evolution during Water Oxidation on the Surface of Perovskite Oxide Catalysts, *J. Phys. Chem. Lett.*, 2012, **3**, 3264–3270.
- 4 E. Fabbri, *et al.*, Dynamic surface self-reconstruction is the key of highly active perovskite nano-electrocatalysts for water splitting, *Nat. Mater.*, 2017, **16**, 925.
- 5 S. H. Chang, *et al.*, Functional links between stability and reactivity of strontium ruthenate single crystals during oxygen evolution, *Nat. Commun.*, 2014, **5**, 4191.
- 6 A. R. Akbashev, *et al.*, Activation of ultrathin SrTiO_3 with subsurface SrRuO_3 for the oxygen evolution reaction, *Energy Environ. Sci.*, 2018, **11**, 1762–1769.
- 7 R. Zhang, *et al.*, A Dissolution/Precipitation Equilibrium on the Surface of Iridium-Based Perovskites Controls Their Activity as Oxygen Evolution Reaction Catalysts in Acidic Media, *Angew. Chem., Int. Ed.*, 2019, **58**, 4571–4575.
- 8 C. W. Song, H. Suh, J. Bak, H. B. Bae and S.-Y. Chung, Dissolution-Induced Surface Roughening and Oxygen Evolution Electrocatalysis of Alkaline-Earth Iridates in Acid, *Chem*, 2019, **5**, 3243–3259.
- 9 R. Zhang, *et al.*, Importance of Water Structure and Catalyst-Electrolyte Interface on the Design of Water Splitting Catalysts, *Chem. Mater.*, 2019, **31**, 8248–8259.
- 10 L. C. Seitz, *et al.*, A highly active and stable $\text{IrO}_x/\text{SrIrO}_3$ catalyst for the oxygen evolution reaction, *Science*, 2016, **353**, 1011.
- 11 N. Danilovic, *et al.*, Activity–Stability Trends for the Oxygen Evolution Reaction on Monometallic Oxides in Acidic Environments, *J. Phys. Chem. Lett.*, 2014, **5**, 2474–2478.
- 12 S. Cherevko, *et al.*, Oxygen and hydrogen evolution reactions on Ru, RuO_2 , Ir, and IrO_2 thin film electrodes in acidic and alkaline electrolytes: A comparative study on activity and stability, *Catal. Today*, 2016, **262**, 170–180.
- 13 S. Cherevko, Stability and dissolution of electrocatalysts: Building the bridge between model and “real world” systems, *Curr. Opin. Electrochem.*, 2018, **8**, 118–125.

- 14 C. Spöri, J. T. H. Kwan, A. Bonakdarpour, D. P. Wilkinson and P. Strasser, The Stability Challenges of Oxygen Evolving Catalysts: Towards a Common Fundamental Understanding and Mitigation of Catalyst Degradation, *Angew. Chem., Int. Ed.*, 2017, **56**, 5994–6021.
- 15 M. Rabe, *et al.*, Alkaline manganese electrochemistry studied by in situ and *operando* spectroscopic methods – metal dissolution, oxide formation and oxygen evolution, *Phys. Chem. Chem. Phys.*, 2019, **21**, 10457–10469.
- 16 C. Roy, *et al.*, Trends in Activity and Dissolution on RuO₂ under Oxygen Evolution Conditions: Particles versus Well-Defined Extended Surfaces, *ACS Energy Lett.*, 2018, **3**, 2045–2051.
- 17 S. Cherevko, S. Geiger, O. Kasian, A. Mingers and K. J. J. Mayrhofer, Oxygen evolution activity and stability of iridium in acidic media. Part 1. – Metallic iridium, *J. Electroanal. Chem.*, 2016, **773**, 69–78.
- 18 S. Cherevko, S. Geiger, O. Kasian, A. Mingers and K. J. J. Mayrhofer, Oxygen evolution activity and stability of iridium in acidic media. Part 2. – Electrochemically grown hydrous iridium oxide, *J. Electroanal. Chem.*, 2016, **774**, 102–110.
- 19 S. Geiger, *et al.*, The stability number as a metric for electrocatalyst stability benchmarking, *Nat. Catal.*, 2018, **1**, 508–515.
- 20 S. Geiger, *et al.*, Activity and Stability of Electrochemically and Thermally Treated Iridium for the Oxygen Evolution Reaction, *J. Electrochem. Soc.*, 2016, **163**, F3132–F3138.
- 21 A. Grimaud, *et al.*, Activation of surface oxygen sites on an iridium-based model catalyst for the oxygen evolution reaction, *Nat. Energy*, 2016, **2**, 16189.
- 22 O. Kasian, *et al.*, Degradation of iridium oxides via oxygen evolution from the lattice: correlating atomic scale structure with reaction mechanisms, *Energy Environ. Sci.*, 2019, **12**, 3548–3555.
- 23 A. Zagalskaya and V. Alexandrov, Role of Defects in the Interplay between Adsorbate Evolving and Lattice Oxygen Mechanisms of the Oxygen Evolution Reaction in RuO₂ and IrO₂, *ACS Catal.*, 2020, **10**, 3650–3657.
- 24 K. Lee, M. Osada, H. Y. Hwang and Y. Hikita, Oxygen Evolution Reaction Activity in IrO_x/SrIrO₃ Catalysts: Correlations between Structural Parameters and the Catalytic Activity, *J. Phys. Chem. Lett.*, 2019, **10**, 1516–1522.
- 25 L. Yang, *et al.*, Efficient oxygen evolution electrocatalysis in acid by a perovskite with face-sharing IrO₆ octahedral dimers, *Nat. Commun.*, 2018, **9**, 5236.
- 26 D.-Y. Kuo, *et al.*, Influence of Strain on the Surface–Oxygen Interaction and the Oxygen Evolution Reaction of SrIrO₃, *J. Phys. Chem. C*, 2018, **122**, 4359–4364.
- 27 G. Wan, *et al.*, Amorphization mechanism of SrIrO₃ electrocatalyst: How oxygen redox initiates ionic diffusion and structural reorganization, *Sci. Adv.*, 2021, **7**, eabc7323.
- 28 Y. Chen, *et al.*, Exceptionally active iridium evolved from a pseudo-cubic perovskite for oxygen evolution in acid, *Nat. Commun.*, 2019, **10**, 572.
- 29 T. Binninger, *et al.*, Thermodynamic explanation of the universal correlation between oxygen evolution activity and corrosion of oxide catalysts, *Sci. Rep.*, 2015, **5**, 12167.
- 30 M. J. N. Pourbaix, J. Van Muylder and N. De Zoubov, Electrochemical properties of the platinum metals, *Platin. Met. Rev.*, 1959, **3**, 47–53.
- 31 P. E. Pearce, *et al.*, Revealing the Reactivity of the Iridium Trioxide Intermediate for the Oxygen Evolution Reaction in Acidic Media, *Chem. Mater.*, 2019, **31**, 5845–5855.
- 32 Z. Wang, X. Guo, J. Montoya and J. K. Nørskov, Predicting aqueous stability of solid with computed Pourbaix diagram using SCAN functional, *npj Comput. Mater.*, 2020, **6**, 160.
- 33 O. Kasian, J.-P. Grote, S. Geiger, S. Cherevko and K. J. J. Mayrhofer, The Common Intermediates of Oxygen Evolution and Dissolution Reactions during Water Electrolysis on Iridium, *Angew. Chem., Int. Ed.*, 2018, **57**, 2488–2491.
- 34 M. Schalenbach, *et al.*, The Electrochemical Dissolution of Noble Metals in Alkaline Media, *Electrocatalysis*, 2018, **9**, 153–161.
- 35 P. Jovanović, *et al.*, Electrochemical Dissolution of Iridium and Iridium Oxide Particles in Acidic Media: Transmission Electron Microscopy, Electrochemical Flow Cell Coupled to Inductively Coupled Plasma Mass Spectrometry, and X-ray Absorption Spectroscopy Study, *J. Am. Chem. Soc.*, 2017, **139**, 12837–12846.
- 36 M. Ben-Naim, *et al.*, Understanding Degradation Mechanisms in SrIrO₃ Oxygen Evolution Electrocatalysts: Chemical and Structural Microscopy at the Nanoscale, *Adv. Funct. Mater.*, 2021, **31**, 2101542.
- 37 Y. Kuwahara, In situ Atomic Force Microscopy study of dissolution of the barite (001) surface in water at 30 °C, *Geochim. Cosmochim. Acta*, 2011, **75**, 41–51.
- 38 K. Miyata, *et al.*, Dissolution Processes at Step Edges of Calcite in Water Investigated by High-Speed Frequency Modulation Atomic Force Microscopy and Simulation, *Nano Lett.*, 2017, **17**, 4083–4089.
- 39 C. Noiriel, M. Oursin, G. Saldi and D. Habertür, Direct Determination of Dissolution Rates at Crystal Surfaces Using 3D X-ray Microtomography, *ACS Earth Space Chem.*, 2019, **3**, 100–108.
- 40 T. Weber, *et al.*, Potential-Induced Pitting Corrosion of an IrO₂(110)–RuO₂(110)/Ru(0001) Model Electrode under Oxygen Evolution Reaction Conditions, *ACS Catal.*, 2019, **9**, 6530–6539.
- 41 C. B. Andersen, Understanding Carbonate Equilibria by Measuring Alkalinity in Experimental and Natural Systems, *J. Geosci. Educ.*, 2002, **50**, 389–403.
- 42 Y. Zhao, N. M. Vargas-Barbosa, E. A. Hernandez-Pagan and T. E. Mallouk, Anodic Deposition of Colloidal Iridium Oxide Thin Films from Hexahydroxyiridate(IV) Solutions, *Small*, 2011, **7**, 2087–2093.
- 43 Y. Zhao, *et al.*, Understanding the Effect of Monomeric Iridium(III/IV) Aquo Complexes on the Photoelectrochemistry of IrO_x·nH₂O-Catalyzed Water-Splitting Systems, *J. Am. Chem. Soc.*, 2015, **137**, 8749–8757.
- 44 M. Pourbaix, *Atlas of Electrochemical Equilibria in Aqueous Solutions*, National Association of Corrosion Engineers, 1966.
- 45 C. Baeumer, *et al.*, Tuning electrochemically driven surface transformation in atomically flat LaNiO₃ thin films for enhanced water electrolysis, *Nat. Mater.*, 2021, **20**, 674–682.

- 46 C. J. Powell, Practical guide for inelastic mean free paths, effective attenuation lengths, mean escape depths, and information depths in X-ray photoelectron spectroscopy, *J. Vac. Sci. Technol., A*, 2020, **38**, 023209.
- 47 S. Tanuma, C. J. Powell and D. R. Penn, Calculations of electron inelastic mean free paths. V. Data for 14 organic compounds over the 50–2000 eV range, *Surf. Interface Anal.*, 1994, **21**, 165–176.
- 48 A. Jablonski and C. J. Powell, Practical expressions for the mean escape depth, the information depth, and the effective attenuation length in Auger-electron spectroscopy and X-ray photoelectron spectroscopy, *J. Vac. Sci. Technol., A*, 2009, **27**, 253–261.
- 49 S. A. Chambers and Y. Du, Experimental determination of electron attenuation lengths in complex materials by means of epitaxial film growth: Advantages and challenges, *J. Vac. Sci. Technol., A*, 2020, **38**, 043409.
- 50 E. Högfeldt, *Stability Constants of Metal–Ion Complexes: Part A. Inorganic Ligands*, Pergamon, 1984.
- 51 E. J. Reardon and D. K. Armstrong, Celestite ($\text{SrSO}_4(\text{s})$) solubility in water, seawater and NaCl solution, *Geochim. Cosmochim. Acta*, 1987, **51**, 63–72.